A Novel Approach for Monitoring The Spatial Distribution and Quantitative Analysis of Micronutrients in Plant Tissues Using Laser Ablation ICP-MS Imaging

DOOLAN, Olivia, PEIRATS-LLOBET, Marta, LEWSEY, Mathew G, ABERDEIN, Nicola and BRICKLEBANK, Neil <http://orcid.org/0000-0002-1614-2260>

Analytical and Bioanalytical Chemistry
https://doi.org/10.1007/s00216-026-06780-z

RESEARCH PAPER

A novel approach for monitoring the spatial distribution and quantitative analysis of micronutrients in plant tissues using laser ablation ICP-MS imaging

Olivia Doolan[1,2] · Marta Peirats-Llobet[2] · Mathew G. Lewsey[2,3,4] · Nicola Aberdein[1] · Neil Bricklebank[1]

Received: 6 July 2026 / Revised: 4 August 2026 / Accepted: 13 August 2026

Abstract

Quantitative imaging of plant tissues by laser ablation inductively coupled plasma mass spectrometry (LA-ICP-MS) is hindered by the lack of matrix-matched calibration standards. Established approaches, such as gelatine or homogenised tissue blocks, do not replicate plant matrices accurately. Here, we introduce a nano-dispenser-based calibration strategy that deposits nanolitre volumes of elemental standards directly onto paraffin-embedded grain sections, exploiting the low endogenous metal content of the endosperm to generate in situ calibration curves. Calibration performance for Mg, Mn, Cu, Zn, and Mo was assessed using LA-ICP-MS imaging and Iolite 4 data processing. The method demonstrated excellent linearity ($R^2 > 0.98$), reproducibility across multiple grains, and sub-ppm limits of detection. Comparative analysis with in-house homogenised blocks and NIST wheat reference material confirmed superior accuracy and reproducibility of the nano-dispenser approach. As a proof-of-concept, we have applied the method for the quantitative imaging of metals in a whole barley grain section, and the results show excellent agreement with published data obtained by conventional liquid-mode ICP MS. The technique reported here provides a robust, scalable, solution for quantitative metallomics studies of plant tissues, enabling improved assessment of nutrient distribution and supporting the development of standardised protocols for LA-ICP-MS imaging.

Keywords Metallomics · Laser ablation · Mass spectrometry/ICP-MS · Bioanalytical methods · Biological samples

Abbreviations

LA-ICP-MS	Laser ablation inductively coupled plasma mass spectrometry
PND	PipeJet nano-dispenser
NIST	National Institute of Standards and Technology
CRMs	Certified reference materials

✉ Neil Bricklebank
n.bricklebank@shu.ac.uk

[1] Biomolecular Sciences Research Centre, Sheffield Hallam University, City Campus, Sheffield S1 1WB, UK

[2] La Trobe Institute for Sustainable Agriculture and Food, Department of Plant, Animal and Soil Sciences, La Trobe University, AgriBio Building, Bundoora, Melbourne, VIC 3086, Australia

[3] Australian Research Council Research Hub for Medicinal Agriculture, La Trobe University, AgriBio Building, Bundoora, Melbourne, VIC 3086, Australia

[4] Australian Research Council Centre of Excellence in Plants for Space, La Trobe University, AgriBio Building, Bundoora, Melbourne, VIC 3086, Australia

Introduction

Laser ablation inductively coupled plasma mass spectrometry (LA-ICP-MS) is a well-established technique for the spatially resolved analysis of endogenous and exogenous elements in solid samples. Key advantages include multi-element capability across a broad dynamic range and minimal sample preparation requirements. Furthermore, the wide spatial resolution range (1–100 µm) and flexibility in laser parameters enable adaptation of laser ablation sampling to diverse sample types [1–6]. Initially developed for applications in geological and materials sciences, LA-ICP-MS has been increasingly applied in the biological sciences, particularly for metallomics investigations in human and animal tissues [7–10].

Since its introduction for bioimaging in 1994 by Wang et al. [11], who demonstrated the use of intrinsic elements such as magnesium and calcium as internal standards to assess signal variability across biological matrices, LA-ICP-MS has advanced considerably [11]. Developments include applications in the study of metal-tagged pharmaceuticals and biomolecules, such as antibodies, enabling

Published online: 08 September 2026

visualisation of their distribution within whole organisms [12–16]. In addition, LA-ICP-MS has been employed to characterise the complete metallome of biological samples, facilitating comparative studies between healthy and diseased tissues [10, 17].

Despite the minimal sample preparation required for LA-ICP-MS, embedding and sectioning of whole organisms are often employed so that specific tissues or regions of interest can be localised. However, these approaches can introduce artefacts, as embedding media, solvent exposure, and dehydration processes may result in redistribution or loss of target analytes.

Accurate quantification by LA-ICP-MS requires appropriate calibration strategies [3, 18]. Matrix-matched calibration standards are particularly important due to matrix effects arising from differences in laser–sample interaction. The ablation efficiency is strongly influenced by the biochemical composition of the sample, which governs laser energy absorption and material ablation [19]. The nature of plant material makes sample preparation complex. The water content in the sample can cause a range of issues from rapid vaporisation in hydrated samples to cell collapse in dry samples [20]. Additionally, variations in sample composition and preparation, including embedding protocols, can therefore affect analyte transport to the ICP-MS and necessitate careful optimisation of laser conditions to ensure complete and reproducible ablation [3, 19, 20].

The development of matrix-matched standards remains a significant challenge. Although a limited number of certified reference materials (CRMs) are available, for example from the National Institute of Standards and Technology (NIST), direct matrix equivalence is often not achievable. Consequently, many laboratories produce in-house standards by homogenising sample tissues and spiking them with known concentrations of elements to generate matrix-matched calibration materials. However, this approach is laborious and can be complicated by the presence of endogenous elements within the tissue prior to spiking [21, 22].

Gelatine-based standards offer advantages such as homogeneity, ease of handling, and low endogenous elemental content, and have gained popularity due to their similarity to mammalian tissue in terms of ablation behaviour [23, 24]. However, gelatine, which is derived from collagen, is not representative of plant matrices [25], limiting its applicability for plant-based studies. Furthermore, gelatine lacks aromatic amino acids and nucleic acids, both of which contribute to absorption of laser energy at 266 nm, resulting in differences in ablation characteristics compared with animal tissues. Plant samples present additional analytical challenges, including structural heterogeneity and variability in tissue composition and size, which can affect laser focus and ablation consistency [26, 27].

Alternative calibration strategies have been explored, including polymer- and resin-based standards [28, 29], solution-based methods [27, 30], and isotope dilution techniques [31]. However, these approaches are often tailored to specific applications and rely on specialised methodologies, limiting inter-laboratory reproducibility and hindering the establishment of universally accepted calibration protocols. Recent reviews have highlighted the advantages and limitations of these strategies in the context of bioimaging [4].

Standard addition is a well-established calibration approach in analytical chemistry. In the broader field of solid-state mass spectrometry imaging, an emerging strategy involves spotting known concentrations of analyte onto control tissues to generate calibration curves [32]. This approach is effective for exogenous analytes, such as pharmaceuticals, where background levels are negligible [33]. However, quantification of endogenous analytes remains challenging due to inherent background signals [32, 33].

In this work, we propose the use of a pipeJET nano-dispenser (PND) to deposit known concentrations of elemental standards directly onto plant tissues, enabling the generation of matrix-matched calibration standards for quantitative LA-ICP-MS. PND systems are high-precision, non-contact liquid handling platforms capable of dispensing nanolitre volumes, and are widely used in life science applications including microarray fabrication and high-throughput screening [34].

This study focuses on metallomics of barley (*Hordeum vulgare*), for which reliable quantitative LA-ICP-MS methodologies are currently limited by the lack of appropriate matrix-matched standards. Barley is often used as a model cereal grain because of its simple diploid genome, self-pollinating nature, and close genetic relationship to complex, polyploid crops like wheat [35, 36]. Furthermore, it is one of the most widely cultivated crops worldwide, with approximately 145 million metric tons harvested annually. It serves as a major food source for humans and animals and is extensively used in the brewing and distilling industries. Figure 1 shows the anatomy of barley, highlighting organs of interest. Herein, we describe a novel approach involving direct spotting of standard solutions onto the endosperm of barley grain sections. The endosperm constitutes the majority of the grain mass but exhibits relatively low metabolic activity and low endogenous metal concentrations, making it an advantageous substrate for calibration. The accuracy of this approach is evaluated through comparison with homogenised, spiked barley tissue standards and by quantification against a NIST certified reference material. We also present data showing the application of the method for the quantitative imaging and speciation of metals in a whole barley grain section. This method lays the groundwork for adaptation, using readily available standards applied to low endogenous metal areas of plant tissue sections.

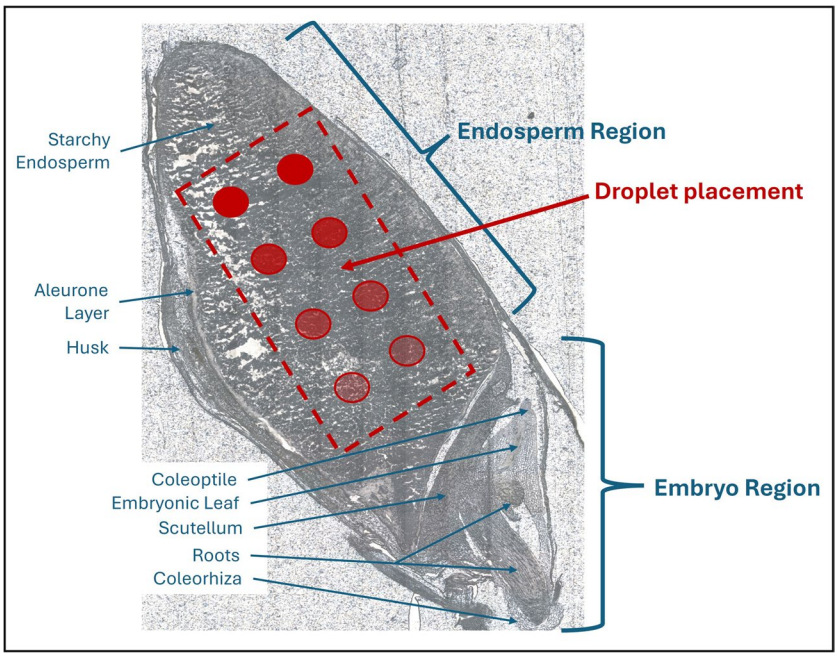

Fig. 1 Optical microscopy image of a paraffin-embedded barley grain at 24 h after imbibition, annotating key regions and organs of interest. Red highlights the region of the grain where droplets were placed for the PND calibration method

Experimental

The approaches used for the preparation of calibration standards in this paper are summarised in Fig. 2.

In-house block calibration method

In order to create a comparative solid-state calibration standard, barley grain powder blocks were produced, comparing the PND calibration method to an established method used in the field. To produce the in-house blocks, grains were washed in deionised water and then freeze-dried at 0.12 mBar and −50 °C until constant mass. Grains were then ground to a fine powder using an electric grinder, then passed through a 40-µm sieve. The grain powder was divided into 1 g aliquots and spiked with an increasing concentration of standard solution. Standard solutions were made up to at least 4 mL with Milli-Q water to ensure the powdered grain was entirely saturated. Each sample was vortexed and then placed on an oscillating table for at least 20 min. All samples were then snap-frozen in liquid nitrogen and stored at −20 °C overnight. The grain slurries were then freeze-dried until constant mass. The dried, ground grain samples were homogenised using a pestle and mortar before being pressed into individual blocks using a 13 mm die at 10 tons of pressure in a hydraulic press for 2 min. The blocks, although delicate, maintain their structure through a combination of mechanical interlocking and intermolecular interaction [37].

Preparation of NIST wheat standards

NIST wheat powder (Standard Reference Material 1567b) was purchased from the National Institute of Standards and Technology for comparison with the in-house calibration blocks and PND calibration method. The NIST wheat standard was used as an 'unknown sample' for comparison to the quantification methods. The NIST wheat was pressed into individual blocks using a 13 mm die at 10 tons of pressure in a hydraulic press for 2 min.

Embedding and sectioning

Grains were processed and embedded in paraffin wax using the protocol established by Liew [38]. For comparison to the PND calibration method, the NIST wheat block was also embedded in paraffin (Leica Microsystems). Paraffin blocks were sectioned at 10 µm using a microtome. Paraffin embedding was chosen over fresh frozen sectioning due to the better quality of section, maintaining the morphology of the grain for more representative imaging.

PND calibration method

Standard solutions were spotted onto barley grain sections using a PND unit (BIOSPOT workstation, Biofluidix). 200-s uncoated pipes were calibrated using the smart drop feature to produce 15 nL spots consistently. Concentrations of standard solutions were tailored by element to apply the most appropriate range for each analyte. The standard solutions used are outlined in Table 1. Standard solutions were diluted

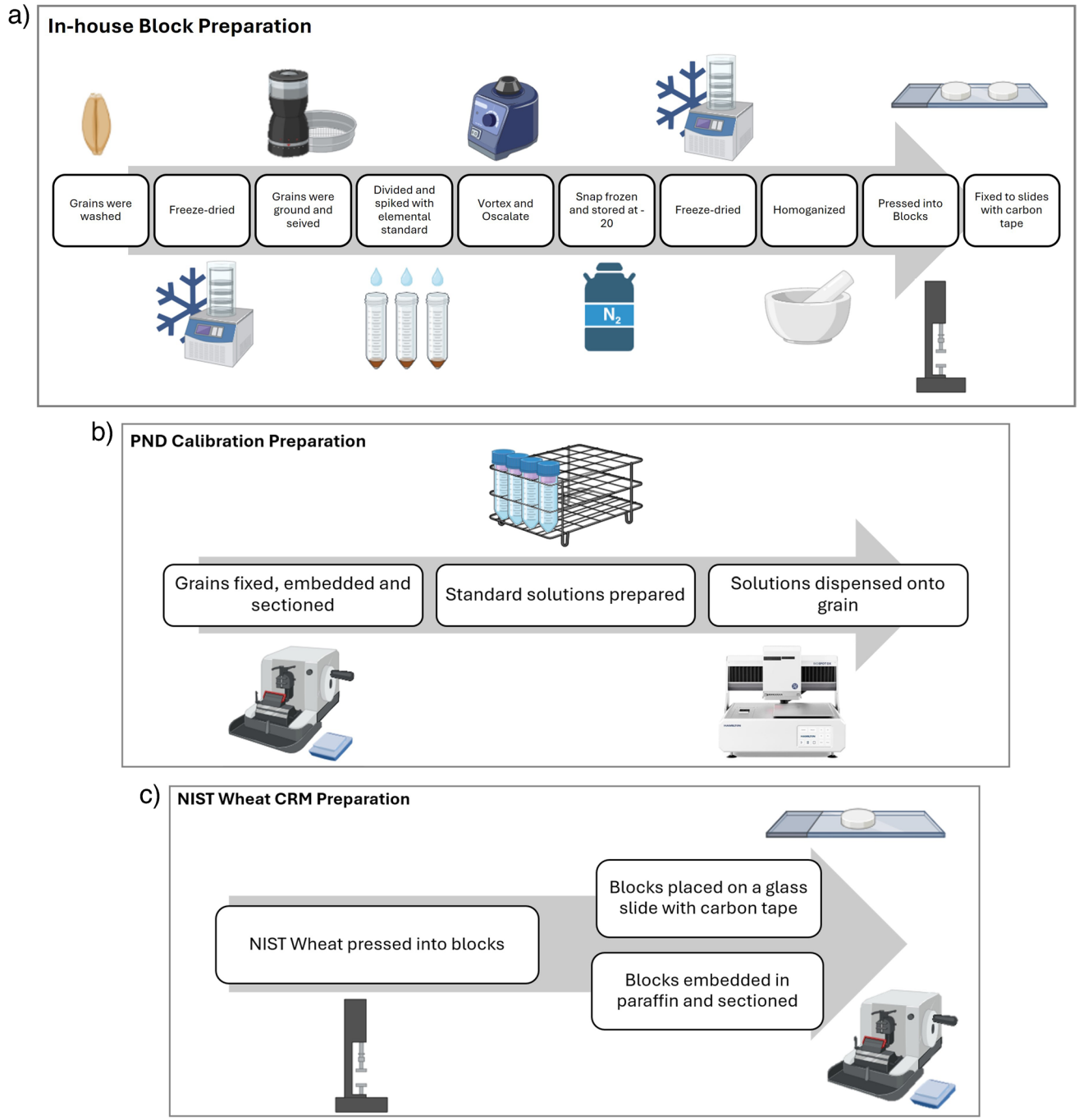

Fig. 2 Comparison of the workflow for our novel PND calibration method with those for established LA-ICP-MS calibration approaches involving production of in-house block standards and use of NIST certified reference materials. **a** Preparation of barley in-house block calibration standards. **b** Preparation of PND spotted calibration standards. **c** Preparation of NIST wheat CRM 'unknown' samples

Table 1 Standard ranges of spotting solutions by element of interest

Element	Concentrations
Magnesium Standard 1000 µg/ml (Spec CertiPrep)	50, 100, 150, 200 ppm
Molybdenum Standard 1000 µg/ml (Spec CertiPrep)	0.05, 0.1, 0.5, 1 ppm
Multi-elemental standard 1000 µg/ml (Copper, Zinc, Manganese) (ThermoFisher)	1, 2, 10, 30 ppm

in 1% nitric acid (trace analysis, ThermoFisher). After spotting, slides were not removed from the PND for ~ 1 min to ensure spots were completely dry. Due to the small volume, spots dried almost instantly after being deposited.

Calibration of the pipeJET nano-dispenser

Before spotting onto a sample, the PND conditions were optimised using the smart drop calibration function within the LifeLAB software (Version: 3.0). Dispensed droplets ($n = 50$) were analysed for volume, size, and shape. The PND achieved this by capturing images of droplets mid-flight with high-speed shutters allowing for accurate droplet calibration. The average and standard deviation were assessed before spots were applied to the barley section (SF1).

Optimisation of PND droplet size

A number of droplet volumes (5 nL, 15 nL, 30 nL, 50 nL) were investigated to find the optimum droplet volume. The 5 and 15 nL droplet volumes were achieved using the 200-s uncoated tips, and the 30 and 50 nL droplet volumes were achieved using the 500-s uncoated tips. The repeatability was assessed using the smart drop feature, where 100 droplet volumes were recorded; the accuracy and precision were determined. The droplets were then spotted onto barley grain sections and imaged using LA-ICP-MS to assess the properties of the droplet, the size, shape, and homogeneity. This was carried out for each elemental group at the highest concentration group (multi-elemental standard, 30 ppm; magnesium, 200 ppm; molybdenum, – 1 ppm).

LA-ICP-MS conditions

Sectioned barley grains, in-house blocks and NIST wheat samples were analysed using an Elemental Scientific 266 ImageBio Laser unit coupled to a PerkinElmer Nexion 5000 ICP mass spectrometer. The Nexion 5000 is a triple quadrupole mass spectrometer with a mass resolving power of < 0.7 amu in each quadrupole. The ImageBio is a 266 nm Nd:YAG laser. Helium carrier gas was used at a flow rate of 800 mL/min in the LA chamber; Ar was introduced at the torch at a rate of around 0.7 ml/min.

The isotopes for analysis were selected carefully (ST1), considering the isotopic abundance and possible polyatomic interferences present in this specific biological sample type.

In order to ensure the optimum operation of the instrument, ICP-MS conditions were tuned on a daily basis, using a solid NIST 612 glass (National Institute of Standards and Technology, Gaithersburg, MD, USA). The NIST glass was used to tune the sampling depth, nebuliser gas flow, torch alignment, and performance of the quadrupole ion deflector (QID). The optimised conditions were decided based on the maximum intensity of ^{115}In and the ratio of ^{238}U to ^{232}Th, as an indication of fractionation.

Spotted grain samples and germinated grain sections were analysed at 25 µm × 25 µm XYR spot size, a repetition rate of 200 Hz, a fluence of 5 J/cm, and a scan speed of 500 µm/s. Laser conditions and ICP-MS dwell times were optimised based on a sigma of 3.291 to give a 99.9% confidence interval.

Three-dimensional trace element analysis

For the LA-ICP-MS data processing, Iolite 4's (Version: 4.10.5) three-dimensional (3D) trace element analysis function was used [39]. A region of interest (ROI) was assigned around each spot. Each ROI was then linked to a specific reference material. The reference materials were manually created in the Iolite reference material tab; values were assigned in femtograms (fg) based on Eq. 1, where the ablated mass was m_p, δ was the thickness of the ablated material (in cm), α was the ablation area (in cm^2), and ρ is the density of the material (in g cm^{-3}).

$$m_p = \delta \times \alpha \times \rho \quad (1)$$

Statistical analysis

Statistical analysis was carried out using GraphPad Prism (Version: 10.4.1). Calibration curves were analysed using simple linear regression analysis. The straight-line fit, the slope difference, and the intercept difference of the curves were compared following statistical analysis outlined by Zar [40]. The droplet size was compared using descriptive statistics.

Results and discussion

Optimisation of droplet volume and spot homogeneity

Droplet volume optimisation was critical to balancing dispensing precision, spot homogeneity, and spatial constraints on the grain surface. Several competing factors were considered. First, droplet formation is inherently influenced by the physicochemical properties of the dispensing solution. In this study, 1% nitric acid was used to stabilise elemental standards and minimise precipitation; however, the relatively high surface tension of water limited droplet reproducibility at lower volumes.

Second, increasing droplet volume improved dispense reliability but introduced artefacts during drying. Larger

droplets exhibited increased lateral spreading prior to drying, resulting in analyte redistribution across the tissue surface. This could be linked to fluid dynamic phenomena such as the Marangoni effect (the 'coffee-ring effect'), whereby surface tension gradients promote solute migration towards droplet edges, leading to inhomogeneous analyte distribution [23, 41].

These effects are evident in Fig. 3a–e, where 30 and 50 nL droplets showed pronounced inhomogeneity compared with 5 and 15 nL droplets. The increased drying time required for the larger volume droplets promoted greater spreading of the solution resulting in spots which were larger, with uneven edges, making droplet drying speed, and therefore volume, a key factor for consideration. In addition, larger droplet

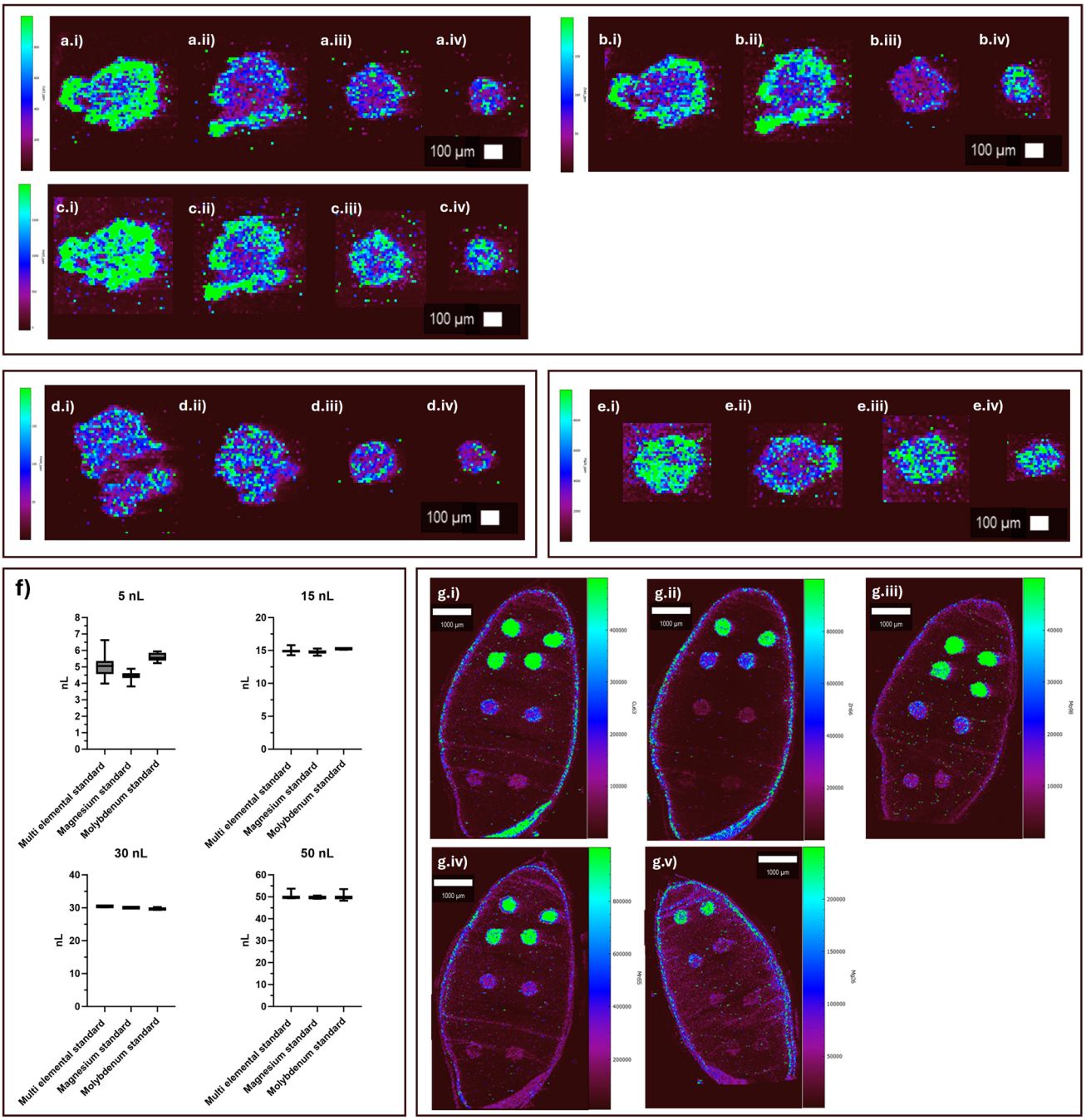

Fig. 3 **a**–**e** LA-ICP-MS images of spots of elemental standard, at varying spot sizes (i. 50 nL, ii. 30 nL, iii. 15 nL, iv. 5 nL), for each element of interest (**a** Cu, **b** Mn, **c** Zn, **d** Mo, **e** Mg). **f** shows the PND reproducibility at different spot sizes for each elemental standard. **g** illustrates how a 15 nL droplet size, four-point calibration curve (in duplicate), was dispensed onto the endosperm of barley for each element of interest (i. Cu, ii. Zn, iii. Mo, iv. Mn, v. Mg)

volumes reduced spatial throughput; increasing droplet size from 15 to 50 nL halved the number of calibration points that could be applied to a single grain.

Droplet reproducibility was assessed using the PND 'smart drop' calibration function ($n = 100$) and was found to improve with increasing volume, with standard deviation decreasing proportionally relative to droplet size (Fig. 3f). However, despite improved precision at higher volumes, the associated loss of spatial resolution and increased inhomogeneity outweighed these benefits.

Collectively, these results demonstrate that droplet volume must be optimised as a compromise between precision, spatial resolution, and homogeneity. Based on these considerations, 15 nL droplets were selected as the optimal condition, providing consistent spot morphology, acceptable reproducibility, and sufficient spatial density for multi-point calibration on individual grain sections (Fig. 3g).

Calibration curve linearity and reproducibility

Calibration performance was assessed using six independent calibration curves (three grains, two replicate curves per grain). All elements exhibited strong linear relationships across the concentration ranges investigated, with mean R^2 values of 0.98–0.99 and low inter-replicate variability.

To plot the calibration lines, the 3D trace elements function in Iolite was used. This utilises fg quantities of elements, the laser spot size, and the density of the material. In this study, the fg, in 15 nL, of each concentration group are as shown in ST 3. The spot size was 25 µm, and the density was set to 1 g/cm^3. The percentage quantity by weight of paraffin was calculated to be 71.8%, making the proportion of plant material to be 28.2%. The density of paraffin is 0.9 g/cm^3, and the density of dried plant material is ~ 1.4 g/cm^3 [42]. Combining these, an overall density of the section of 1 g/cm^3 was assumed (SF2).

As shown in Fig. 4 and Table 2, statistical comparison of regression parameters demonstrated no significant differences in slope or intercept for Zn, Cu, Mn, and Mg ($P > 0.05$), indicating excellent reproducibility across independent measurements. This confirms that the PND-based approach produces highly consistent calibration behaviour across multiple sections and experimental runs. The slope quantifies the steepness of the curve, and the intercept is where the curve crosses the *Y*-axis. By using both these variables, it was determined that the lines were statistically identical and not distinct but parallel. The slope of Molybdenum ($R^2 = 0.98 \pm 0.02$) did significantly differ ($P = 0.032$). However, considering the low concentrations used in this calibration range, it is expected to see more variability. Nonetheless, the lines still show a good linear relationship and that they are somewhat reproducible. It is noted that the *Y*-intercept values for these calibration curves are large. This is likely due to background interference. Every ICP-MS has a level of background counts, contributed by a combination of residual analyte in the system and plasma-generated ions. However, there may be some additional factors to consider such as residual memory effects between ablation lines, drift in signal, and the level of endogenous metal in the 'blank' tissues. When using biological tissues, it is difficult to obtain a matrix that is entirely free of trace amounts of metallic elements; however, there is the potential for low levels of metals to be present in the endosperm. However, the endosperm offers a relative 'blank tissue' in comparison to the other tissues in the grain. Residual analysis further supported the robustness of the calibration model, with evenly distributed residuals and no evidence of systematic bias or outliers (SF3).

Together, these results demonstrate that the PND calibration strategy yields highly reproducible and linear calibration curves suitable for quantitative LA-ICP-MS imaging of plant tissues.

Comparative quantitative methods

Evaluation of calibration accuracy is inherently challenging for droplet-based approaches. More traditional tissue-type or gelatine-based methods can be assessed for accuracy using liquid (ICP-MS)-based techniques, where the tissue or gelatine standards are digested and analysed against a set of known standard solutions [21, 23]. However, the nature of the PND calibration standards means that an alternative method to assess its accuracy must be employed.

To do this, we used a NIST certified reference material as a solid-state 'unknown' to be analysed using LA-ICP-MS. The lack of availability of CRMs is a limitation of LA-ICP-MS, and at the time of the experiment, there was no available NIST standard for barley; therefore, we chose wheat as a comparable grain. Barley and wheat are from the same biological family and are chemically similar, nutrient-dense, cereal grains with high levels of carbohydrates. The NIST wheat was pressed into blocks using the same method used to prepare the in-house calibration blocks.

In order to successfully compare the in-house blocks to the PND method, there were a number of variables to be considered. The first is the variability in sample yield (ablation efficiency), which refers to the amount of solid material removed from the sample surface per laser pulse that is subsequently transported to the ICP-MS for analysis. The embedded grains were sectioned at 10 µm thickness and mounted onto glass slides. This combined with the nature of the 266 nm laser system results in a constant sample yield both throughout sampling and between samples. However, the in-house blocks are densely packed and have no limit to the depth of laser penetrating the sample. This results in variation in sample yield between blocks, due to minor

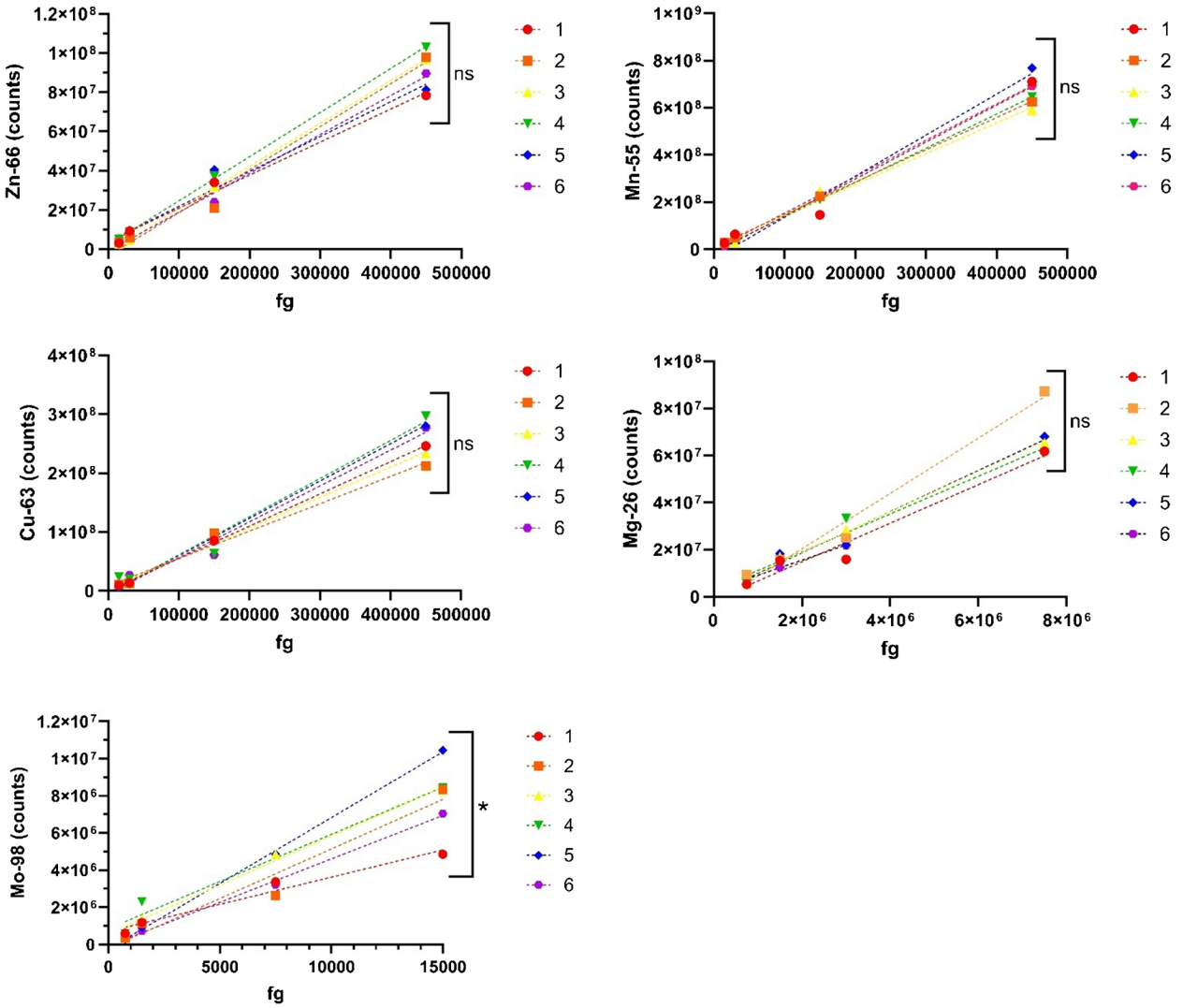

Fig. 4 Calibration curves created using the PND on barley endosperms for Zn, Cu, Mn, Mo, and Mg. $n = 6$, $^*P < 0.05$

variations in density of the blocks and from small fluctuations in laser fluence. This fluctuation has been documented by Mervič et al., who used electron microscopy to identify ablation volumes for quantitative LA-ICP-MS [43, 44]. Therefore, it would not be a fair assessment to compare the NIST wheat block directly to the PND method where the standards were spotted onto paraffin-embedded grain sections. In order to overcome this, we placed a NIST wheat block in paraffin and sectioned it; this allows for a better comparison to the PND calibration curve.

Normalisation of in-house calibration curves was required to compensate for variability in ablation yield and endogenous elemental content. The calibration curves were normalised to the highest concentration group. Doing this improved the linearity and intercept values of the curves. This was required due to the variation in laser sampling yields between blocks and the presence of endogenous metals in the grain powder before spiking. The normalised curves were then used to calculate the output from the NIST wheat blocks. In contrast, the PND calibration curves did not benefit from normalisation, reflecting their inherent reproducibility and consistency. Calibration curves used can be found in the supplementary information (SF4 and SF5).

Figure 5 illustrates the calculated concentrations in ppm from Iolite of the in-house blocks compared to the NIST wheat block and the PND calibration curve to the embedded NIST wheat section. The ablation lines were run in triplicate and repeated on different days, giving 6 individual calculated values for each calibration method. Quantitative comparison (Fig. 5) demonstrated that concentrations derived using the PND method were not significantly different from certified values for Zn, Cu, Mn, and Mg, whereas the in-house block method showed significant deviations.

Table 2 Statistical analysis of calibration curves in Fig. 3

		Average	Standard deviation	Difference of slope	Difference of intercept
Zn-66	*R* squared	0.989	0.011	$P=0.72$	$P=0.56$
	Slope	201.117	21.593		
	Y-intercept	802,555.667	2,805,826.866		
Cu-65	*R* squared	0.988	0.010	$P=0.088$	$P=0.76$
	Slope	569.933	65.737		
	Y-intercept	132,003.833	4,655,044.136		
Mn-55	*R* squared	0.990	0.010	$P=0.16$	$P=0.97$
	Slope	1496.667	142.487		
	Y-intercept	−6,377,636.167	17,475,070.857		
Mg-26	*R* squared	0.980	0.013	$P=0.12$	$P=0.35$
	Slope	8.615	1.598		
	Y-intercept	687,555.833	2,276,839.322		
Mo-98	*R* squared	0.980	0.018	$P=0.032$	-
	Slope	506.117	121.749		
	Y-intercept	264,183.000	446,970.062		

For Mo, both methods exhibited deviation from certified values, although the discrepancy was markedly greater for the in-house approach.

Although the in-house block calibration used here has been successfully applied within the field of quantitative LA-ICP-MS for many years, there are limitations [2, 22]. The variability in yield, non-comparability to sectioned samples, the presence of endogenous metals in homogenised tissue, and laborious preparation limit the application of this quantitative method. The development of gelatine microdroplet standards has advanced quantitative LA-ICP-MS of mammalian tissues. However, in the field of quantitative plant material imaging, these advancements have yet to be realised as the gelatine standards are not an ideal matrix-match for plant tissues.

Quantitative imaging of barley

The optimised PND calibration method was applied to quantify elemental distributions in germinating barley grains at 0 and 24 h after imbibition (HAI). The resulting images (Fig. 6) reveal both spatial distribution and quantitative changes in elemental abundance during early germination.

Elemental redistribution is clearly observed in metabolically active tissues, particularly within the embryo region, reflecting increased demand for micronutrients involved in enzymatic and biochemical processes during germination. Importantly, these measurements capture redistribution within the grain without external nutrient input, highlighting the internal mobilisation of stored elements.

The overall concentration of elements in the grain is highly dependent on the development conditions of the grain and the genotype. A previous study by Lombi et al. [45] used liquid-mode ICP to determine the levels of Mg, Mn, Cu, and Zn in barley grains that had been separated into nine fractions: hull, embryo, core endosperm, and six samples across the testa aleurone–endosperm interface. High-definition synchrotron X-ray fluorescence was also used to generate elemental distribution maps of a longitudinal section of a barley grain [45]. Lombi and coworkers found the levels of Mg, Zn, and Cu in the embryo to be 2000, 120, and 20 μg g^{-1}, respectively. From the quantitative images acquired using our method (Fig. 5), we estimate ~ 2000 μg g^{-1} of Mg, ~ 150 μg g^{-1} of Zn, and ~ 25 μg g^{-1} of Cu in the embryo tissues. Our results reported here are in very close agreement with the data reported by Lombi [45]. For manganese, Lombi reported a level of ~ 150 μg g^{-1} in the embryo of the grains and ~ 20 μg g^{-1} in the whole grain. This is higher than the levels quantified in our grain embryos using our method, which indicated a Mn concentration of ~ 30 μg g^{-1}. Unfortunately, Mo was not reported by Lombi and coworkers, but overall concentrations of Mo in plant tissue have been reported to be between 0.1 and 2.0 μg g^{-1} [46], and the value of ~ 2 μg g^{-1} which we have found in this study falls within this range.

These results demonstrate that the PND calibration strategy enables reliable quantitative imaging of plant tissues, providing both spatial and numerical insight into metallomic processes during development.

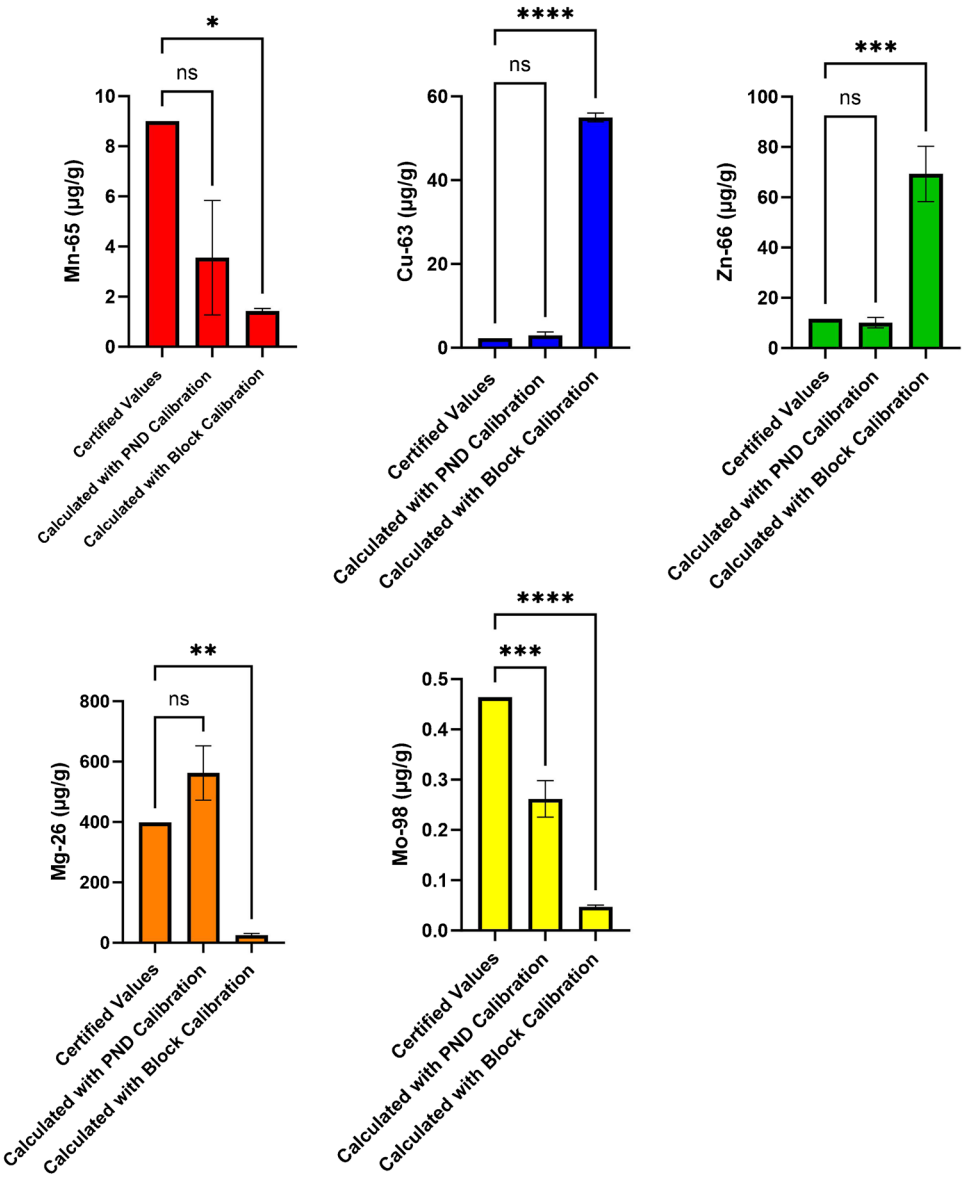

Fig. 5 Comparison of calibration methods for LA-ICP-MS quantitative analysis. Comparing the ppm quantity of each metal on the NIST certified reference material to calculated values using the PND and in-house block calibration methods

Conclusion

In this work, we present a novel calibration strategy for quantitative LA-ICP-MS imaging of paraffin-embedded plant tissues. By exploiting the low endogenous metal content of the endosperm, the direct deposition of standard solutions using a pipeJET nano-dispenser enables the generation of in situ matrix-matched calibration curves. This approach provides both accurate quantification and spatially resolved information on elemental distributions within biological samples.

Barley grains represent a suitable model system for this methodology, as the structural characteristics of the grain—particularly the endosperm—allow reproducible placement of calibration standards with minimal interference from endogenous metals. The PND-based approach demonstrated superior accuracy and reproducibility compared with conventional in-house homogenised calibration blocks, which are limited by variability in ablation yield, incomplete matrix matching, and laborious preparation.

While tissue-matched calibration strategies have been successfully applied in LA-ICP-MS, their translation to sectioned biological samples remains challenging. In contrast, the method presented here directly integrates calibration into the sample itself, improving compatibility with standard preparation workflows and reducing sources of analytical variability.

Current developments in quantitative mass spectrometry imaging, particularly gelatine micro-droplet approaches, have advanced the field considerably for mammalian systems [23, 47]. However, these strategies are not readily transferable to plant tissues due to differences in matrix

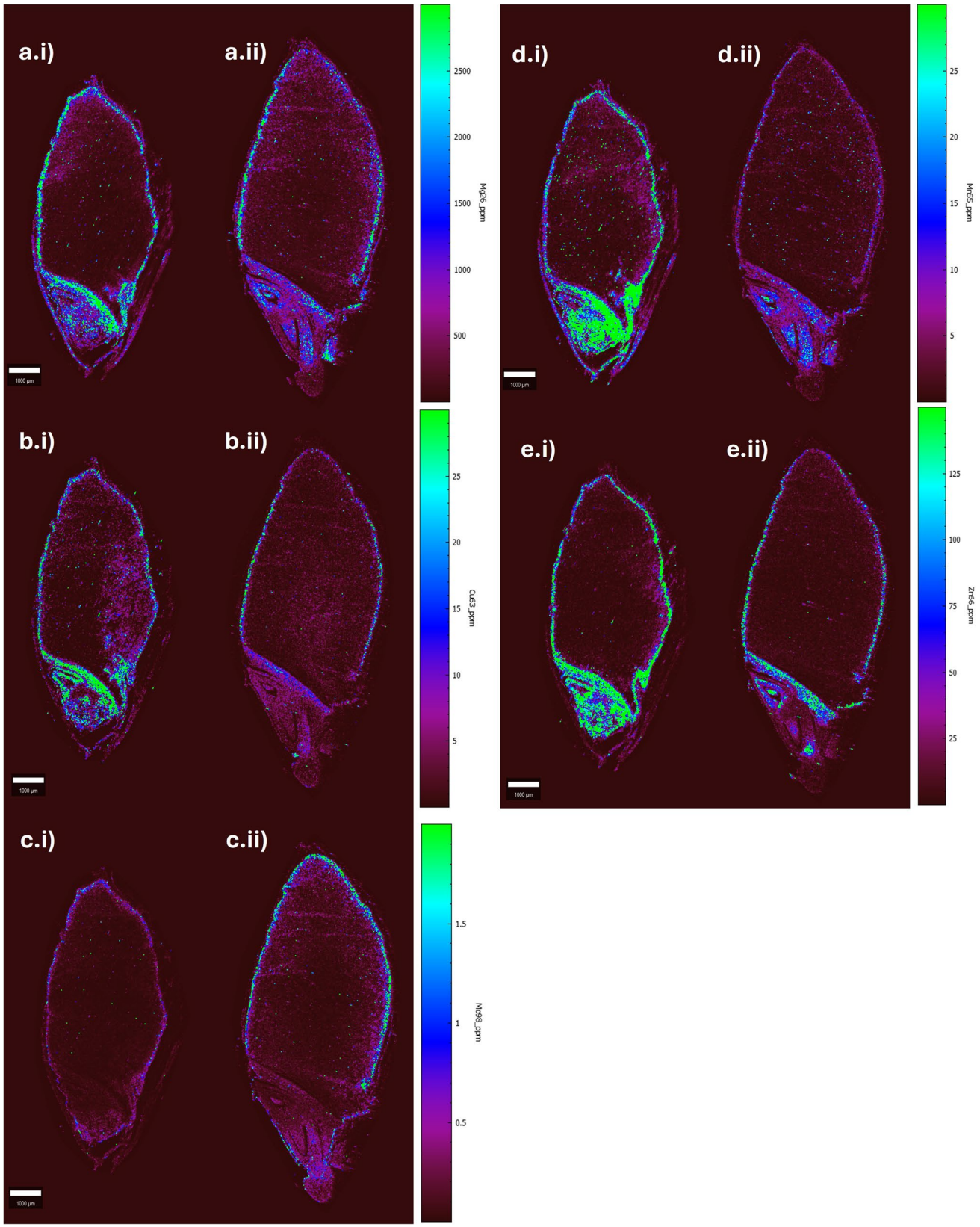

Fig. 6 Quantitative LA-ICP-MS images acquired using the PND calibration method for each element of interest (**a** Mg, **b** Cu, **c** Mo, **d** Mn, **e** Zn) at 0 HAI (i) and 24 HAI (ii)

composition and optical properties. The PND-based calibration method addresses this gap by providing a more representative matrix-match for plant samples.

Although absolute quantification in biological tissues remains inherently limited by sample preparation artefacts and matrix-dependent effects, the approach described here offers a robust and reproducible framework for comparative metallomics. It enables reliable determination of elemental concentrations in paraffin-embedded plant tissues and facilitates the study of dynamic processes such as nutrient redistribution during germination.

Importantly, this method is readily adaptable and utilises commercially available instrumentation, supporting broader adoption across laboratories. Beyond barley, the approach has potential applicability to a wide range of plant and biological tissues where suitable calibration strategies are currently lacking, thereby contributing to the ongoing development of standardised methodologies for quantitative LA-ICP-MS imaging.

Supplementary Information The online version contains supplementary material available at https://doi.org/10.1007/s00216-026-06780-z.

Acknowledgements The authors would like to thank Sheffield Hallam and La Trobe University for funding this research through the provision of a studentship for OD.

Author contribution OD: data collection, writing the original manuscript draft and editing; NB and NA: supervision and reviewing and editing the draft manuscript. ML and MP-L reviewed the draft manuscript.

Data availability The datasets used and/or analysed during the present study are stored in the Sheffield Hallam SHURA data repository and can be made available by contacting the corresponding author upon reasonable request.

Declarations

Conflict of interest The authors declare no competing interests.

References

1. Bishop DP, Clases D, Fryer F, Williams E, Wilkins S, Hare DJ, et al. Elemental bio-imaging using laser ablation–triple quadrupole–ICP-MS. J Anal At Spectrom. 2016;31:197.
2. Van Malderen SJM, Laforce B, Van Acker T, Vincze L, Vanhaecke F. Imaging the 3D trace metal and metalloid distribution in mature wheat and rye grains via laser ablation-ICP-mass spectrometry and micro-X-ray fluorescence spectrometry. J Anal At Spectrom. 2017;32:289–98.
3. Pan H, Feng L, Lu Y, Han Y, Xiong J, Li H. Calibration strategies for laser ablation ICP-MS in biological studies: a review. TrAC Trends Anal Chem. 2022. https://doi.org/10.1016/j.trac.2022.116710.
4. Mervič K, Šala M, Theiner S. Calibration approaches in laser ablation inductively coupled plasma mass spectrometry for bioimaging applications. TrAC Trends in Analytical Chemistry. 2024. https://doi.org/10.1016/j.trac.2024.117574.
5. Sajnóg A, Hanć A, Barałkiewicz D. Metrological approach to quantitative analysis of clinical samples by LA-ICP-MS: a critical review of recent studies. Talanta. 2018. https://doi.org/10.1016/j.talanta.2018.01.050.
6. Chew D, Drost K, Marsh JH, Petrus JA. LA-ICP-MS imaging in the geosciences and its applications to geochronology. Chem Geol. 2021;559:119917.
7. Metarapi D, Schweikert A, Jerše A, Schaier M, van Elteren JT, Koellensperger G, et al. Semiquantitative analysis for high-speed mapping applications of biological samples using LA-ICP-TOFMS. Anal Chem. 2023;95:7804–12.
8. Cui Z, He M, Chen B, Hu B. In-situ elemental quantitative imaging in plant leaves by LA-ICP-MS with matrix-matching external calibration. Anal Chim Acta. 2023;1275:341588.
9. Hosseinpour Mashkani SM, Bishop DP, Raoufi-Rad N, Adlard PA, Shimoni O, Golzan SM. Distribution of copper, iron, and zinc in the retina, hippocampus, and cortex of the transgenic APP/PS1 mouse model of Alzheimer's disease. Cells. 2023. https://doi.org/10.3390/cells12081144.
10. Wang S, Brown R, Gray DJ. Application of LA-ICP-MS to spatially resolved micro-analysis of biological tissue. Appl Spectrosc. 1994;48:1321–5.
11. Van Malderen SJM, Managh AJ, Sharp BL, Vanhaecke F. Recent developments in rapid response cells for LA-ICP-MS and their impact on bioimaging. J Anal At Spectrom. 2016;31:423–39.
12. Timerbaev AR. Recent progress of ICP-MS in the development of metal-based drugs and diagnostic agents. J Anal At Spectrom. 2014;29:1058–72.
13. Theiner S, Schreiber-Brynzak E, Jakupec MA, Galanski M, Koellensperger G, Keppler BK. LA-ICP-MS imaging in multicellular tumor spheroids. Metallomics. 2016;8:398–402.
14. Razumienko E, Ornatsky O, Kinach R, Milyavsky M, Lechman E, Baranov V, et al. Element-tagged immunoassay with ICP-MS detection. J Immunol Methods. 2008;336:56–63.
15. Seiffert SB, Vennemann A, Nordhorn ID, Kröger S, Wiemann M, Karst U. LA-ICP-MS and lanthanide-labeled antibodies for CeO_2 nanoparticle uptake. Chem Res Toxicol. 2022;35:981–91.
16. Paul B, Hare DJ, Bishop DP, Paton C, Nguyen VT, Cole N, et al. Visualising mouse neuroanatomy and function by metal distribution using LA-ICP-MS imaging. Chem Sci. 2015;6:5383–93.
17. Limbeck A, Galler P, Bonta M, Bauer G, Nischkauer W, Vanhaecke F. Recent advances in quantitative LA-ICP-MS analysis: challenges and solutions in the life sciences and environmental chemistry. Anal Bioanal Chem. 2015;407:6593–617. https://doi.org/10.1007/s00216-015-8858-0.
18. Meng J, Lü T, Fang B, Ni Y, Fan B. Laser sampling and matrix effects in LA-ICP-MS. Opt Laser Technol. 2022;152:108092.
19. Ko JA, Furuta N, Lim HB. Quantitative mapping of elements in basil leaves (*Ocimum basilicum*) based on cesium concentration and growth period using laser ablation ICP-MS. Chemosphere. 2018;190:368–74. https://doi.org/10.1016/j.chemosphere.2017.10.003.

20. Becker P, Nauser T, Wiggenhauser M, Aeschlimann B, Frossard E, Günther D. In vitro fossilization for high spatial resolution quantification of elements in plant-tissue using LA-ICP-TOFMS. Anal Chem. 2024. https://doi.org/10.1021/acs.analchem.3c05849.
21. Hare DJ, Lear J, Bishop D, Beavis A, Doble PA. Protocol for production of matrix-matched brain tissue standards for imaging by laser ablation–inductively coupled plasma–mass spectrometry. Anal Methods. 2013;5:1915–21. https://doi.org/10.1039/C3AY26248K.
22. Schweikert A, Theiner S, Wernitznig D, Schoeberl A, Schaier M, Neumayer S, et al. Micro-droplet–based calibration for LA-ICP-MS. Anal Bioanal Chem. 2022;414:485–95.
23. Peng CA, Kozubowski L, Marcotte J, William R. Advances in plant-derived scaffold proteins. Front Plant Sci. 2020;11:122.
24. Šala M, Šelih VS, van Elteren JT. Gelatin gels as multi-element calibration standards in LA-ICP-MS bioimaging: fabrication of homogeneous standards and micro homogeneity. 2017. https://doi.org/10.1039/c7an01361b.
25. Nunes MAG, Voss M, Corazza G, Flores EMM, Dressler VL. External calibration strategy for trace element quantification in botanical samples by LA-ICP-MS using filter paper. Anal Chim Acta. 2016;905:51–7. https://doi.org/10.1016/j.aca.2015.11.049.
26. Bonta M, Hegedus B, Limbeck A. Application of dried-droplets deposited on pre-cut filter paper disks for quantitative LA-ICP-MS imaging of biologically relevant minor and trace elements in tissue samples. Anal Chim Acta. 2016;908:54–62. https://doi.org/10.1016/j.aca.2015.12.048.
27. Austin C, Hare D, Rawling T, McDonagh AM, Doble P. Quantification using metal-spiked PMMA films. J Anal At Spectrom. 2010;25:722–5.
28. Reifschneider O, Wehe CA, Raj I, Ehmcke J, Ciarimboli G, Sperling M, et al. Quantitative platinum bioimaging in polymer-embedded organs. Metallomics. 2013;5:1440–7.
29. O'Connor C, Landon MR, Sharp BL. Absorption coefficient modified pressed powders for calibration of laser ablation inductively coupled plasma mass spectrometry. J Anal At Spectrom. 2007;22:273–82.
30. O'Connor C, Sharp BL, Evans P. Online liquid additions for LA-ICP-MS calibration. J Anal At Spectrom. 2006;21:556–65.
31. Liu J, Zheng L, Li Q, Feng L, Wang B, Chen M, et al. Isotope dilution LA-ICP-MS for mouse brain imaging. Anal Chim Acta. 2023;1273:341524.
32. Tobias F, Hummon AB. Considerations for MALDI-based quantitative mass spectrometry imaging studies. J Proteome Res. 2020;19:3620–30. https://doi.org/10.1021/acs.jproteome.0c00443.
33. Shariatgorji R, Niehues M, Nilsson A, Angerer T, Stroth N, Paslawski W, et al. Quantitative mass spectrometry imaging protocols for spatially heterogeneous samples. Anal Chem. 2025;97:10957–61. https://doi.org/10.1021/acs.analchem.5c00677.
34. Hamilton Company. BIOSPOT workstation product page [Internet]. 2025 [cited 2026 Feb 13]. https://www.hamiltoncompany.com/ultra-low-volume/biospot-workstation. Accessed 3/9/2026.
35. Rotasperti L, Sansoni F, Mizzotti C, Tadini L, Pesaresi P. Barley's second spring as a model organism for chloroplast research. Plants. 2020. https://doi.org/10.3390/plants9070803.
36. Sato K. History and future perspectives of barley genomics. DNA Res. 2020. https://doi.org/10.1093/dnares/dsaa023.
37. Fox C, Bastawros K, Magrini T, Daraio C. Controllable interlocking in two-phase composites. Matter. 2025:102201. https://doi.org/10.1016/j.matt.2025.102201
38. Liew LC, Narsai R, Wang Y, Berkowitz O, Whelan J, Lewsey MG. Temporal transcriptome regulation during barley germination. Plant J. 2020;101:700–15.
39. Paul B, Petrus J, Savard D, Woodhead J, Hergt J, Greig A, et al. Time-resolved trace element calibration strategies for LA-ICP-MS. J Anal At Spectrom. 2023;38:1995–2006.
40. Zar J. Comparing simple linear regression equations. In: Biostatistical Analysis, Pearson Education, UK, 2013. pp. 319–409.
41. Hu H, Larson RG. Marangoni effect reverses coffee-ring depositions. J Phys Chem B. 2006;110:7090–4.
42. Chang CS. Measuring density and porosity of grain kernels using a gas pycnometer. Cereal Chem. 1988;65:13–15.
43. Mervič K, van Elteren JT, Bele M, Šala M. Utilizing ablation volume for calibration in LA-ICP-MS mapping to address variations in ablation rates within and between matrices. Talanta. 2024. https://doi.org/10.1016/j.talanta.2023.125379.
44. Mervič K, Šelih VS, Šala M, van Elteren JT. Non-matrix-matched calibration in bulk multi-element laser ablation – inductively coupled plasma – mass spectrometry analysis of diverse materials. Talanta. 2024. https://doi.org/10.1016/j.talanta.2024.125712.
45. Lombi E, Smith E, Hansen TH, Paterson D, de Jonge MD, Howard DL, et al. Megapixel imaging of (micro)nutrients in mature barley grains. J Exp Bot. 2011;62:273–82.
46. Barros JAVA, Virgilio A, Schiavo D, Nóbrega JA. Determination of ultra-trace levels of Mo in plants by inductively coupled plasma tandem mass spectrometry (ICP-MS/MS). Microchem J. 2017;133:567–71.
47. Braun G, Schaier M, Werner P, Theiner S, Zanghellini J, Wisgrill L, et al. MeXpose: a modular imaging pipeline for cellular metal bioaccumulation. JACS Au. 2024;4:2197–210.